



Seismic source characterization of the Arabian Peninsula and Zagros Mountains from regional moment tensor and coda envelopes

Andrea Chiang¹ · Rengin Gök¹ · Yahya M. Tarabulsi² · Salah Y. El-Hadidy³ · Wael W. Raddadi² · Abdullah D. Mousa²

Received: 14 April 2020 / Accepted: 14 November 2020 / Published online: 6 January 2021
 © Saudi Society for Geosciences 2021

Abstract

Reliable estimates of moment magnitude and source mechanism for seismic events in the Middle East can be challenging due to a small number of openly available stations, the complex tectonic setting, and regions of high attenuation. Access to high-quality waveform data from well-calibrated regional seismic stations is fundamental in producing robust and stable estimates of earthquake source parameters, particularly when measurements of absolute ground motion amplitudes are required. Earthquake source mechanism and moment magnitude are invaluable information in the assessment of seismic hazard, plate motions, and the characterization of faults and regional stress field. The expansion of the Kingdom of Saudi Arabia's national seismic network in the past several decades provides an opportunity to develop the capabilities of routine focal mechanism and moment magnitude estimations. In this study, we use time-domain full waveform moment tensor inversion and coda envelope-derived amplitude measurements to solve for earthquake source mechanism, moment magnitudes, and their source type. We compared the moment magnitudes calculated from the two methods and publicly available earthquake catalogs and discuss the implications of the obtained source parameters.

Keywords Moment tensor · Moment magnitude · Coda · Earthquake source · Middle East

Introduction

Reliable estimates of moment magnitude (M_w) and source mechanism for seismic events in the Middle East can be challenging due to a small number of openly available stations, the complex tectonic setting, and regions of high attenuation (Rodgers et al. 1997; Mitchell et al. 1997; Cong and Mitchell 1999). Access to high-quality waveform data from well-calibrated regional seismic stations is fundamental in

producing robust and stable estimates of earthquake source parameters, particularly when measurements of absolute ground motion amplitudes are required. Source mechanism and magnitude are invaluable information in the assessment of seismic hazard, plate motions, and the characterization of faults and regional stress field. In the Kingdom of Saudi Arabia, there are also renewed public safety concerns near historically inactive lava fields due to a recent 2009 earthquake swarm in northwestern part of the country. Location,

This article is part of the Topical Collection on *Seismic and Earthquake Engineering Studies in the Arabian Plate and the Surrounding Region*

✉ Andrea Chiang
 Chiang4@llnl.gov

Rengin Gök
 gok1@llnl.gov

Yahya M. Tarabulsi
 tarabulsi.ym@sgs.org.sa

Salah Y. El-Hadidy
 salah_elhadidy@nriag.sci.eg

Wael W. Raddadi
 raddadi.ww@sgs.org.sa

Abdullah D. Mousa
 mousa.ad@sgs.org.sa

¹ Lawrence Livermore National Laboratory, 7000 East Avenue, Livermore, CA L-043, USA

² Saudi Geological Survey, P.O. Box 54141, Jeddah 21514, Saudi Arabia

³ National Research Institute of Astronomy and Geophysics, EL Marsad Street 1 Helwan, Cairo, Egypt

size, and mechanism of seismicity associated with magma flow are important information used to assess potential risks of volcanic eruptions and hazard related to volcanic earthquake swarms. Abundant low-magnitude seismic events accompanying magma intrusions means lowering the monitoring threshold is crucial to capture all the seismicity, thus data collected from regional networks and local arrays play an important role.

The Middle East is a tectonically diverse region of active seismicity and complex geology due to the presence of all major types of plate boundaries resulting from interactions between five major tectonic plates: Eurasia, Arabia, Sinai, Somali, and India (Reilinger et al. 2006). Our study area focuses on the Arabian Peninsula and parts of the Iranian Plateau and can be divided into three major tectonic regions from east to west: (1) Zagros fold-and-thrust belt, (2) Arabian platform and shield, and (3) Red Sea Rift Zone. Starting from the east of our study region (Fig. 1), convergence between Eurasia and Arabian plate is accommodated largely by intracontinental shortening along major mountain belts within

Iran, and to the southeast, the relative motion of the Arabian plate to Eurasia is accommodated by the Makran subduction zone (Regard et al. 2004) where the Arabian plate subducts underneath Eurasia along the Gulf of Oman. Following the collision zone from southeastern Turkey to Iran's western border, the 2000-km-long Zagros fold-and-thrust belt is the largest and most active collisional orogeny in the region (Mouthereau et al. 2012). Deformation in the Zagros is segmented into several domains due to past collisional orogenies and reactivation of old features during present-day plate convergence. Zagros fold-and-thrust belt is dominated by reverse faulting but strike-slip faulting is not uncommon and not necessarily confined to narrow zones of major strike-slip faults (Berberian 1981). Across the Gulf, the Arabian Peninsula can be divided into the western Arabian Shield and the eastern Arabian Platform. The Shield is made of accreted Proterozoic island arc terranes with little to no sediments above the basement crystalline rocks; in contrast, the Platform is covered with Phanerozoic sediments as thick as 10 km deep (Stoeser and Camp 1985). Around 30-Ma rifting

Fig. 1 Map of the study region.

A topographic and bathymetric map showing the Arabian Peninsula and surrounding regions. The black polygons outline two major tectonic features: the Arabian shield to the west and the Zagros fold-and-thrust belt to the east (Pollastro et al. 1999). The circles are earthquakes from Table 1 color-coded by depth and the size of circles corresponds to their magnitude. The white squares are broadband seismic stations used for moment tensor inversions. National boundaries and coastlines are plotted as gray lines

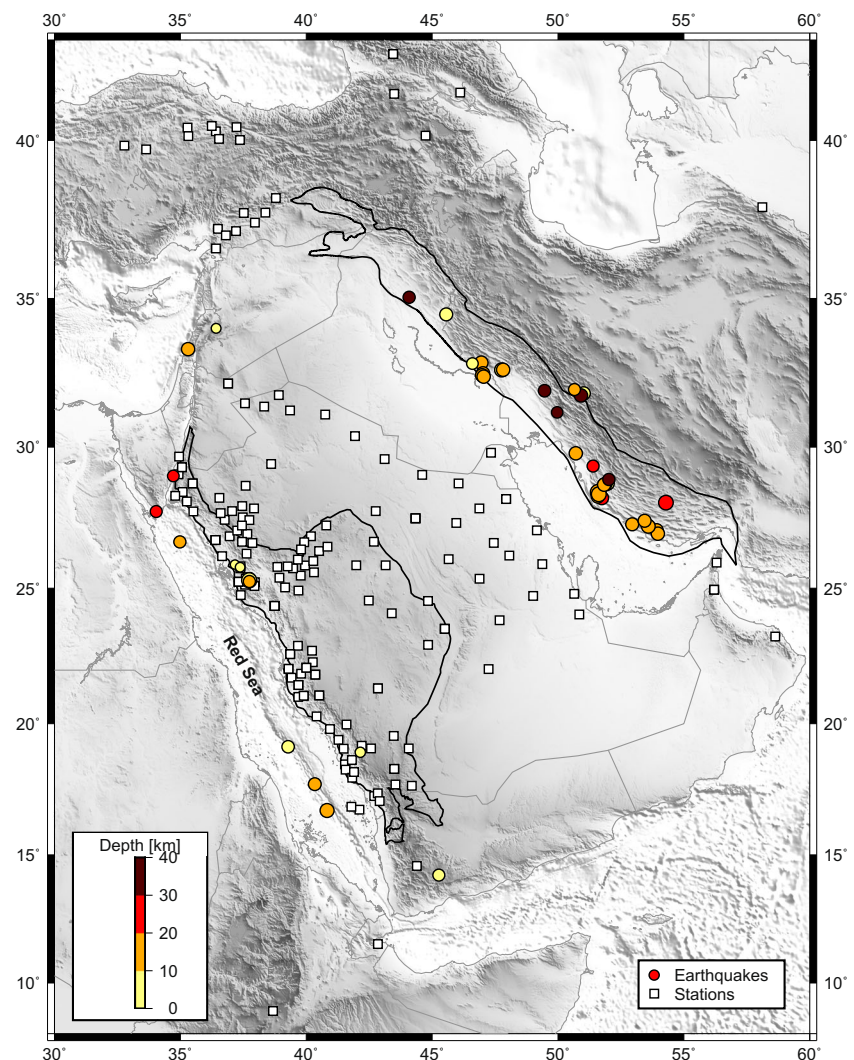


Table 1 Earthquake origin time and locations

No.	Date	Time	Longitude	Latitude	Depth ^a	Mb	Catalog	Region
1	2011-10-19	02:52:43.20	54.286	28.058	23.4	5.5	NEIC	Zagros
2	2012-03-05	06:50:37.94	44.095	35.042	32.1	4.6	NEIC	Zagros
3	2012-03-08	18:21:38.50	46.957	32.874	18	5.1	NEIC	Zagros
4	2012-04-20	01:21:07.54	47.023	32.511	10	5.1	NEIC	Zagros
5	2012-04-20	03:05:41.78	46.99	32.453	10	5	NEIC	Zagros
6	2012-04-21	05:25:08.41	47.049	32.407	10	5	NEIC	Zagros
7	2012-05-13	18:21:13.43	53.923	27.086	10	4.9	NEIC	Zagros
8	2012-06-08	16:15:14.80	50.705	29.784	14.6	5	NEIC	Zagros
9	2012-07-01	02:49:46.00	51.02	31.841	6.6	5	NEIC	Zagros
10	2012-09-06	03:43:40.09	53.97	26.96	16	5	NEIC	Zagros
11	2013-01-25	12:11:27.92	50.913	31.769	37.7	5	NEIC	Zagros
12	2013-04-09	11:52:49.92	51.593	28.428	12	5.9	NEIC	Zagros
13	2013-05-01	18:31:05.90	51.741	28.229	23.8	5.1	NEIC	Zagros
14	2013-05-23	22:44:56.90	53.588	27.221	18.1	5.2	NEIC	Zagros
15	2014-08-18	18:08:21.75	47.7628	32.6305	0	5.3	IDC	Zagros
16	2014-08-20	10:14:16.88	47.8207	32.6394	18.7	5	IDC	Zagros
17	2013-04-10	01:00:20.00	51.584	28.275	18	4.9	NEIC	Zagros
18	2013-04-10	01:58:27.20	51.62	28.355	15	5.6	NEIC	Zagros
19	2013-11-22	06:51:23.90	45.5608	34.48	0	4.9	IDC	Zagros
20	2014-12-30	04:19:33.79	51.9659	28.7386	0	5.1	IDC	Zagros
21	2015-01-01	08:49:54.26	51.8723	28.7076	15.3	5.1	ISC	Zagros
22	2015-01-10	17:03:07.87	51.8335	28.693	10.3	5	ISC	Zagros
23	2015-04-12	16:48:16.66	52.9513	27.2959	11.6	4.9	ISC	Zagros
24	2015-04-29	02:37:46.18	53.4398	27.4204	11.9	4.9	ISC	Zagros
25	2015-09-25	06:10:22.26	46.5988	32.8449	0	4.4	IDC	Zagros
26	2015-11-25	21:17:21.58	49.4697	31.9284	38.3	4.7	IDC	Zagros
27	2015-12-04	19:23:17.30	52.0189	28.8721	33.3	4.6	IDC	Zagros
28	2016-03-31	07:15:18.55	50.6568	31.9721	16.5	4.5	IDC	Zagros
29	2016-07-02	03:49:50.86	51.392	29.3414	28.6	4.5	IDC	Zagros
30	2016-10-14	01:43:53.82	49.9636	31.1905	38.9	4.3	IDC	Zagros
31	2007-05-09	18:45:19.77	34.979	26.672	10	4.6	NEIC	Red Sea
32	2012-01-30	17:04:28.21	34.0397	27.7453	25.4	4.5	ISC	Red Sea
33	2013-07-08	15:30:28.06	40.831	16.707	10.5	5.3	NEIC	Red Sea
34	2013-12-23	18:44:20.43	39.2791	19.1333	0	4.7	IDC	Red Sea
35	2016-03-07	22:43:24.99	40.3359	17.7165	10	4.8	NEIC	Red Sea
36	2009-05-17	19:20:08.86	37.745	25.378	10	4	NEIC	Lunayyir
37	2009-05-17	20:21:07.71	37.724	25.338	10	4	NEIC	Lunayyir
38	2009-05-19	17:35:01.07	37.74	25.291	5	5.7	NEIC	Lunayyir
39	2009-05-19	19:57:18.35	37.745	25.243	10	4.6	NEIC	Lunayyir
40	2017-03-10	05:37:30.84	37.1678	25.855	0	3.5	IDC	Arabian Peninsula
41	2017-04-03	20:18:56.11	37.3727	25.7592	6.36	3.6	SGS	Arabian Peninsula
42	2017-11-03	01:06:51.88	42.15	18.9233	0	3.9	IDC	Arabian Peninsula
43	2008-02-15	10:36:19.09	35.305	33.327	10	5	NEIC	Arabian Peninsula
44	2014-09-01	20:50:05.80	36.4209	34.0248	0	3.7	IDC	Arabian Peninsula
45	2015-06-27	15:34:03.72	34.7214	28.9983	24.3	4.4	IDC	Arabian Peninsula
46	2016-05-24	17:43:27.91	45.2702	14.2195	0	4.5	IDC	Arabian Peninsula

IDC International Data Centre, ISC International Seismological Centre, NEIC National Earthquake Information Center, SGS Saudi Geological Survey

^a Source depth in kilometers

Table 2 Earthquake source parameters

No.	Depth	Mw	Mo	Mxx	Myy	Mzz	Mxy	Mxz	Myz	Coda Mw
1	8	5	3.89E + 23	- 3.44E + 23	8.27E + 22	2.61E + 23	- 1.45E + 23	1.56E + 22	- 2.01E + 22	5.08
2	21	5.1	5.56E + 23	7.66E + 21	- 2.51E + 22	1.75E + 22	- 4.99E + 23	- 1.09E + 23	1.58E + 23	5.17
3	22	4.8	2.06E + 23	7.01E + 22	- 7.70E + 22	6.88E + 21	1.12E + 23	- 1.14E + 23	- 4.46E + 22	4.92
4	8	5.1	4.61E + 23	- 2.74E + 23	- 1.02E+23	3.77E + 23	- 1.80E + 23	2.31E + 23	9.62E + 22	5.07
5	8	5.1	5.10E + 23	- 2.88E + 23	- 8.86E + 22	3.77E + 23	- 1.78E + 23	2.59E + 23	1.96E + 23	5.11
6	7	4.9	2.29E + 23	- 1.18E + 23	- 5.39E+22	1.71E + 23	- 7.37E + 22	1.30E + 23	7.54E + 22	4.88
7	7	5.1	5.41E + 23	- 3.22E + 23	- 8.93E + 22	4.12E + 23	- 1.14E + 23	3.06E + 23	1.54E + 23	5.05
8	8	4.9	2.31E + 23	- 7.80E + 22	- 6.09E + 22	1.39E + 23	- 1.24E + 23	5.41E + 22	1.13E + 23	4.81
9	5	5	2.95E + 23	- 2.09E + 23	5.34E + 20	2.08E + 23	2.04E + 22	1.64E + 23	- 1.05E + 23	4.87
10	7	4.8	1.60E + 23	2.65E + 22	1.10E + 23	- 1.36E + 23	- 4.70E + 22	1.21E + 22	- 7.99E + 22	4.76
11	7	4.9	2.39E + 23	- 1.73E + 23	- 8.16E + 20	1.74E + 23	- 1.40E + 22	1.54E + 23	4.71E + 22	4.86
12	8	6.3	2.73E + 25	- 5.64E + 24	- 1.25E + 25	1.82E + 25	- 1.69E + 25	8.07E + 24	1.91E + 24	6.26
13	4	4.8	1.93E + 23	- 1.26E+23	- 4.01E + 22	1.66E + 23	- 8.77E + 22	8.04E + 22	- 1.51E + 22	4.9
14	12	4.4	4.61E + 22	- 1.52E + 21	- 1.13E + 22	1.28E + 22	- 1.05E + 22	2.56E + 21	- 4.22E + 22	4.59
15	7	6	1.25E + 25	- 6.44E + 24	- 1.40E + 24	7.84E + 24	- 2.90E + 24	9.37E + 24	2.06E + 24	6.01
16	16	5.5	2.23E + 24	- 1.31E + 24	- 7.25E + 23	2.03E + 24	- 6.38E + 23	7.95E + 23	3.75E + 23	5.5
17	6	4.6	8.87E + 22	- 6.07E + 22	4.63E + 22	1.44E + 22	- 2.87E + 22	4.30E + 22	- 3.95E + 22	4.65
18	4	5.4	1.58E + 24	- 7.97E + 23	- 2.26E + 23	1.02E + 24	- 9.66E + 23	3.24E + 22	6.05E + 23	5.56
19	14	5.5	2.06E + 24	- 6.31E + 23	- 9.38E + 23	1.57E + 24	- 1.03E + 24	4.45E + 23	8.32E + 23	5.59
20	4	5	3.61E + 23	1.23E + 23	- 1.10E + 23	- 1.32E + 22	- 5.54E + 22	- 2.29E + 23	- 2.16E + 23	5.03
21	2	4.8	1.50E + 23	- 6.43E + 21	- 2.00E + 22	2.64E + 22	1.11E + 22	- 1.25E + 23	- 5.29E + 22	4.73
22	6	4.6	9.41E + 22	5.59E + 22	- 6.72E + 22	1.12E + 22	- 1.87E + 22	- 2.43E + 21	5.12E + 22	4.72
23	6	5	3.20E + 23	- 1.08E + 23	- 4.50E + 22	1.54E + 23	- 7.89E + 22	2.39E + 23	1.35E + 23	4.94
24	10	4.7	1.39E + 23	- 1.06E + 23	- 1.13E + 22	1.17E + 23	- 3.13E + 22	7.36E + 22	7.04E + 21	4.79
25	9	5	3.52E + 23	- 7.00E + 22	- 8.56E + 22	1.56E + 23	2.13E + 22	2.34E + 23	1.58E + 23	5.08
26	2	5.2	7.27E + 23	- 1.18E + 23	- 1.32E + 23	2.50E + 23	2.27E + 22	9.24E + 23	7.47E + 23	5.03
27	2	5	3.52E + 23	- 3.90E + 22	- 2.87E + 22	6.77E + 22	- 1.53E + 22	- 2.96E + 23	- 1.63E + 23	4.59
28	19	4.8	1.61E+23	- 1.39E + 23	1.47E + 23	- 8.08E + 21	- 1.26E + 22	2.58E + 22	- 4.77E + 22	4.87
29	10	4.3	3.02E + 22	- 1.20E + 21	- 1.59E + 22	1.71E + 22	- 1.41E + 22	1.25E + 22	1.16E + 22	4.38
30	21	4.5	5.67E + 22	- 2.11E+22	- 3.32E + 22	5.42E + 22	- 6.94E + 21	1.26E+22	- 4.63E + 21	
31	13	4.4	4.55E + 22	- 3.58E + 21	- 1.94E + 22	2.29E + 22	2.22E + 22	6.22E + 21	- 2.95E + 22	
32	8	4.8	1.60E + 23	2.87E + 22	7.10E + 22	- 9.97E + 22	3.01E + 22	- 6.86E + 22	- 9.97E + 22	4.58
33	6	5.6	2.69E+24	- 2.79E + 23	1.06E + 24	- 7.78E + 23	9.20E + 23	- 4.90E + 23	2.29E+24	5.6
34	6	5.3	9.12E + 23	4.06E + 23	3.52E + 23	- 7.58E + 23	1.40E + 23	3.30E + 23	3.33E + 23	5.21
35	9	5	3.36E + 23	1.29E + 23	1.36E + 23	- 2.65E + 23	4.62E + 22	1.11E + 23	1.55E + 23	4.87

Table 2 (continued)

No.	Depth	Mw	Mo	Mxx	Myx	Mzz	Mxy	Mxz	Myz	Coda Mw
36	8	3.8	6.54E + 21	- 1.93E + 21	1.26E + 21	6.75E + 20	5.54E + 21	- 5.13E + 20	2.22E + 21	
37	8	4.1	1.40E + 22	- 8.09E + 20	7.98E + 21	- 7.17E + 21	7.62E + 21	- 1.25E + 21	7.18E + 21	
38	4	5.7	4.55E + 24	1.42E + 24	2.24E + 24	- 3.66E + 24	1.53E + 24	5.92E + 23	2.46E + 24	5.74
39	5	4.8	1.85E + 23	5.77E + 22	6.24E + 22	- 1.20E + 23	5.68E + 22	2.68E + 22	1.27E + 23	4.75
40	5	3.7	4.24E + 21	1.07E + 21	1.41E + 21	- 2.48E + 21	1.86E + 21	2.57E + 21	1.34E + 21	
41	6	3.4	1.61E + 21	4.78E + 20	3.10E + 20	- 7.88E + 20	5.26E + 20	1.29E + 21	1.30E + 20	
42	9	3.9	8.59E + 21	7.87E + 21	- 6.46E + 21	- 1.41E + 21	- 3.30E + 21	3.79E + 20	1.30E + 21	
43	9	5.1	5.30E + 23	3.50E + 23	- 2.61E + 23	- 8.93E + 22	3.03E + 23	1.13E + 23	2.04E + 23	
44	24	3.6	3.12E + 21	1.76E + 20	5.63E + 20	- 7.39E + 20	2.74E + 21	7.65E + 20	- 8.87E + 20	
45	17	5.5	1.88E + 24	- 9.95E + 23	9.95E + 23	3.99E + 20	1.55E + 24	2.04E + 23	- 1.39E + 23	
46	24	4.7	1.43E + 23	9.26E + 22	- 1.12E + 23	1.91E + 22	8.51E + 22	5.96E + 21	1.27E + 22	

began and propagated east- and north-ward to form the Gulf of Aden and the Red Sea, respectively (Camp and Roobol 1992). Rifting of the Red Sea is associated with extensive uplift and volcanism and formation of Harrat lava fields throughout the Arabian Shield. Between April and July 2009, a seismic swarm of more than 30,000 earthquakes occurred beneath one of the smallest lava fields in the Arabian Shield, Harrat Lunayyir. The lava field is located near the northern Red Sea on a passive margin where seafloor spreading has not developed (Hansen et al. 2007). While the most recent volcanic eruption was more than 1000 years ago (Camp et al. 1987, p. 1987), there are occasional seismic swarms interpreted as fracturing of crystalline basement rocks during episodes of magma intrusions (Pallister et al. 2010). Two major sets of faults have been observed in northwestern Saudi Arabia including reactivated NE-SW trending Precambrian faults due to rifting of the Red Sea and NW-SE trending faults subparallel to rifting (Mukhopadhyay et al. 2013).

The booming urban development and occasional volcanic swarms near major cities in Saudi Arabia contributed to a renewed interest in understanding seismic hazard and risk to the community, which led to the expansion of Saudi Arabia's national seismic network in the past several decades. The collection of local and regional data provides an opportunity to develop the capabilities of routine focal mechanism and Mw estimations for the country. This study is not only to support the operational needs to national networks in Saudi Arabia but also to obtain stable and robust solutions that give quantitative information about the seismicity needed to better understand potential seismic hazards, local and regional tectonics, and in situ stress fields of the region. In this study we use time-domain full waveform moment tensor inversion to solve for source parameters of earthquakes and identify their source type, and a subset of those events we apply the coda calibration technique to obtain coda envelope-based Mw. Unlike full waveform modeling methods, coda waves are insensitive to the propagation and source radiation effects on moment estimation. Therefore, the analysis of stable coda envelope amplitudes compared with regional moment tensor inversions provides an independent check on the scalar seismic moment biases. In addition, we also compared source parameters to other published earthquake catalogs to examine the similarities and differences and discuss the tectonic implications of the obtained source parameters.

Data

We use a collection of open- and closed-source three-component broadband seismic data from regional seismic networks (Fig. 1). The majority of the data are closed to the public and come from the Saudi National Seismic Network (SNSN); the network is operated by the National Center for Earthquakes

and Volcanoes at the Saudi Geological Survey (SGS). The center monitors seismicity and volcanic activities within and around Saudi Arabia. Open source data come from regional seismic networks in Georgia, Jordan, Kuwait, Oman, and Turkey and stations part of the Global Seismic Network (GSN). Publicly available waveforms and metadata are archived at the Incorporated Research Institutions for Seismology (IRIS; last accessed online June 17, 2019). For the moment tensor analysis, we consider 46 earthquakes recorded by SNSN between 2007 and 2017, where data were made available to us by the SGS. The majority of the events analyzed are moderate- to large-sized earthquakes ($4 < M < 6$) located along the seismically active Zagros fold-and-thrust belt, and a dozen or so earthquakes recorded in Western Arabian Peninsula and Red Sea (Fig. 1 and Table 1). Four earthquakes located in northwest Saudi Arabia are part of the 2009 Harrat Lunayyir seismic swarm, in which additional permanent telemetered broadband stations were installed as a result of the volcanic activity (Pallister et al. 2010). Of the 46 earthquakes in Table 1, we calculate M_w for 36 events using the coda calibration technique. Calibrations are done in two distinct tectonic regions (Zagros and Red Sea) where we have enough events to select a few large events for calibration to obtain the necessary correction terms, and apply the corrections to the rest of the data and independently calculate M_w .

Method: moment tensor inversion

For each earthquake, we perform three-component, time-domain, full waveform moment tensor inversion to estimate the following source parameters: focal mechanism, total seismic moment, and source depth. The inversion is based on the mathematical formulation defined in (Minson and Dreger 2008) to allow for calculation of the full moment tensor (hence isotropic components) and details of the procedure is described in previous works such as Dreger (2003) and Chiang et al. (2016). In summary, the seismic moment tensor approximates the source as an equivalent body force system that produces displacements identical to those from the actual forces at the source. Using this mathematical point force representation of the seismic source, the recorded seismograms can be modeled as the linear combination of weighted basis Green's functions. The Green's functions describe the impulse response of the Earth at the seismic station for a point force applied at the source, including near-, intermediate-, and far-field terms for body and surfaces waves, and the weights on these Green's functions are the individual moment tensor elements (Jost and Herrmann 1989). In this study, we assume the source time function to be a delta function. The Green's functions are

calculated based on the frequency-wavenumber integration method, using a wave propagation solver from the software package called Computer Programs in Seismology (Herrmann 2013). The generation of Green's functions requires a subsurface velocity model. For this study, we use a 1-D Gulf model (Rodgers et al. 1999) for earthquakes originating from the Zagros fold-and-thrust belt and a 1-D Arabian Shield model (Pasyanos et al. 2004) for earthquakes from Western Arabian Peninsula and Red Sea Rift Zone. Rodgers et al. (1999) found that crustal attenuation does not strongly affect surface wave amplitudes greater than 10-s periods, so we fixed the crustal Q_s and Q_p to 200 and 400, respectively.

Data are instrument corrected to ground displacement, rotated to the great-circle-path, decimated, and filtered between 0.02 and 1 Hz. The zerophase, three-pole, Butterworth-Bandpass filter corner frequencies are chosen based on the size of the earthquake, the recording distance, and the signal-to-noise ratios (SNR). The same filtering and down-sampling parameters are applied to the synthetic seismograms. The processed data are then inverted for deviatoric and full moment tensor solutions. The additional

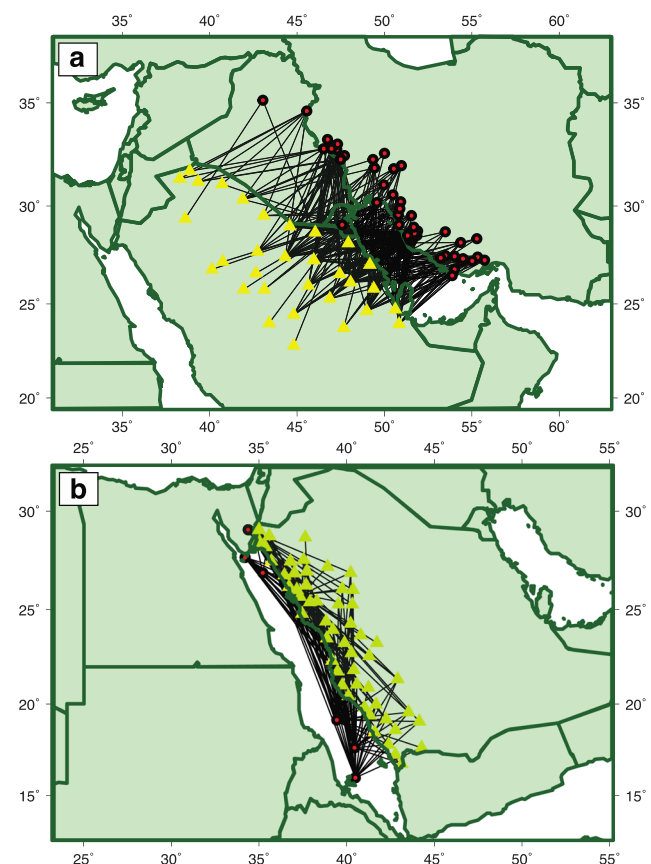


Fig. 2 Coda calibration map. Ray paths of the two calibration subregions (a) Zagros and (b) Red Sea. The red circles are the earthquakes, the yellow triangles are stations used in the Zagros subregion calibration, and the green triangles are stations used in the Red Sea subregion calibration

degree-of-freedom in full moment tensor inversion is required to describe events with isotropic components (often interpreted as volume change in the source) such as mining explosion and collapse, and needed to represent solutions in the source-type framework. We determine the source depth using a grid-search approach in which the deviatoric solution with the highest goodness-of-fit parameter (variance reduction, VR) between data and synthetic seismograms is selected as the preferred solution. From the full moment tensor solution, we calculate the source-type parameters γ and δ for each event based on a geometric framework of moment tensors on a three-dimensional unit sphere (Tape and Tape 2012). Source-type plots have been used to display inferred source types of seismic events, including earthquakes, volcanic events, mine collapses, and explosions (Ford et al. 2009) and can be used as a framework for varied data-type inversions and assessment of recoverability and confidence in moment tensor solutions under various inversion conditions (Nayak and Dreger 2018; Chiang et al. 2018).

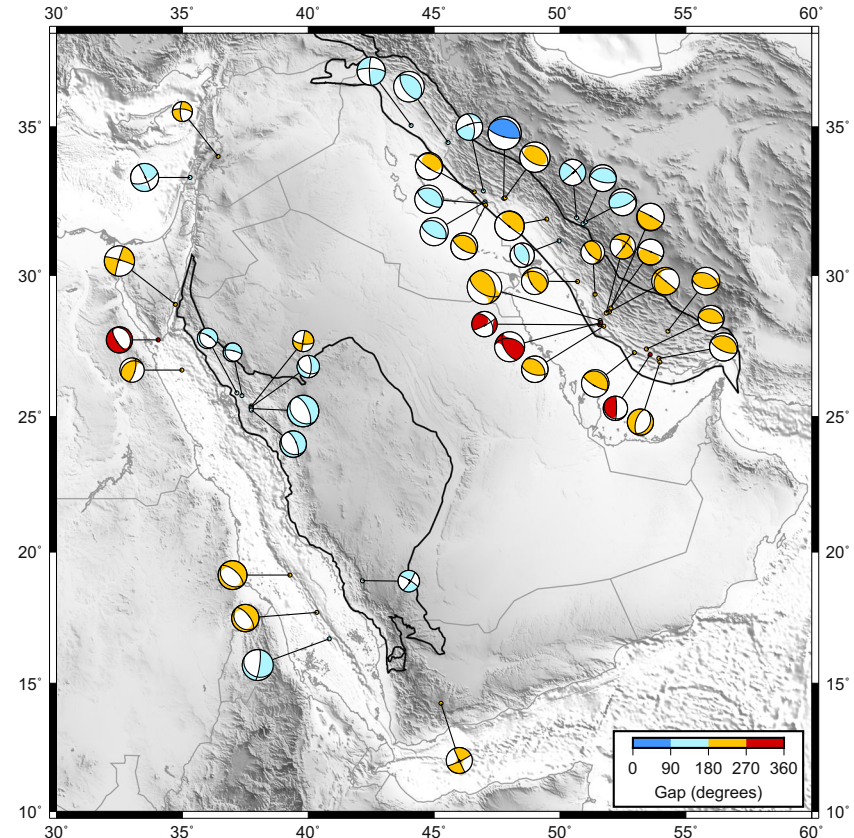
Method: coda calibration technique

Seismic moment derived from regional waveform modeling such as moment tensor inversion depends

heavily on knowledge of the subsurface velocity structure to calculate the synthetic basis Green's functions. The challenge of this waveform modeling approach is not all regions around the globe have suitable Earth models that can be used to remove the wave propagation effects between the source and receiver. Any uncertainty in the subsurface structure can lead to incorrect or biased moment tensor results. The analysis of stable coda envelope amplitudes compared with regional moment tensor inversions provides an independent check on the scalar seismic moment biases. In previous studies, we found that coda envelope amplitude measurements were not very sensitive to 3D path heterogeneities at low frequencies (below 0.7 Hz) and source radiation pattern, provided that ample duration was available for the amplitude measurements (Mayeda and Malagnini 2010). Because of the scattering nature of the coda, amplitudes were derived from the envelopes average over the path and source variation. The resultant source spectra can then be used to calculate stable moment estimates (and hence Mw). Previous results demonstrated that applying empirical 1-D path correction for different regions in coda-based method can produce stable amplitude estimates.

A reliable source spectrum is difficult to obtain from direct phases because amplitudes of direct phases

Fig. 3 Focal mechanisms. Focal mechanisms of the 46 earthquakes from deviatoric moment tensor inversion. The beach balls are color-coded according to their azimuthal gap



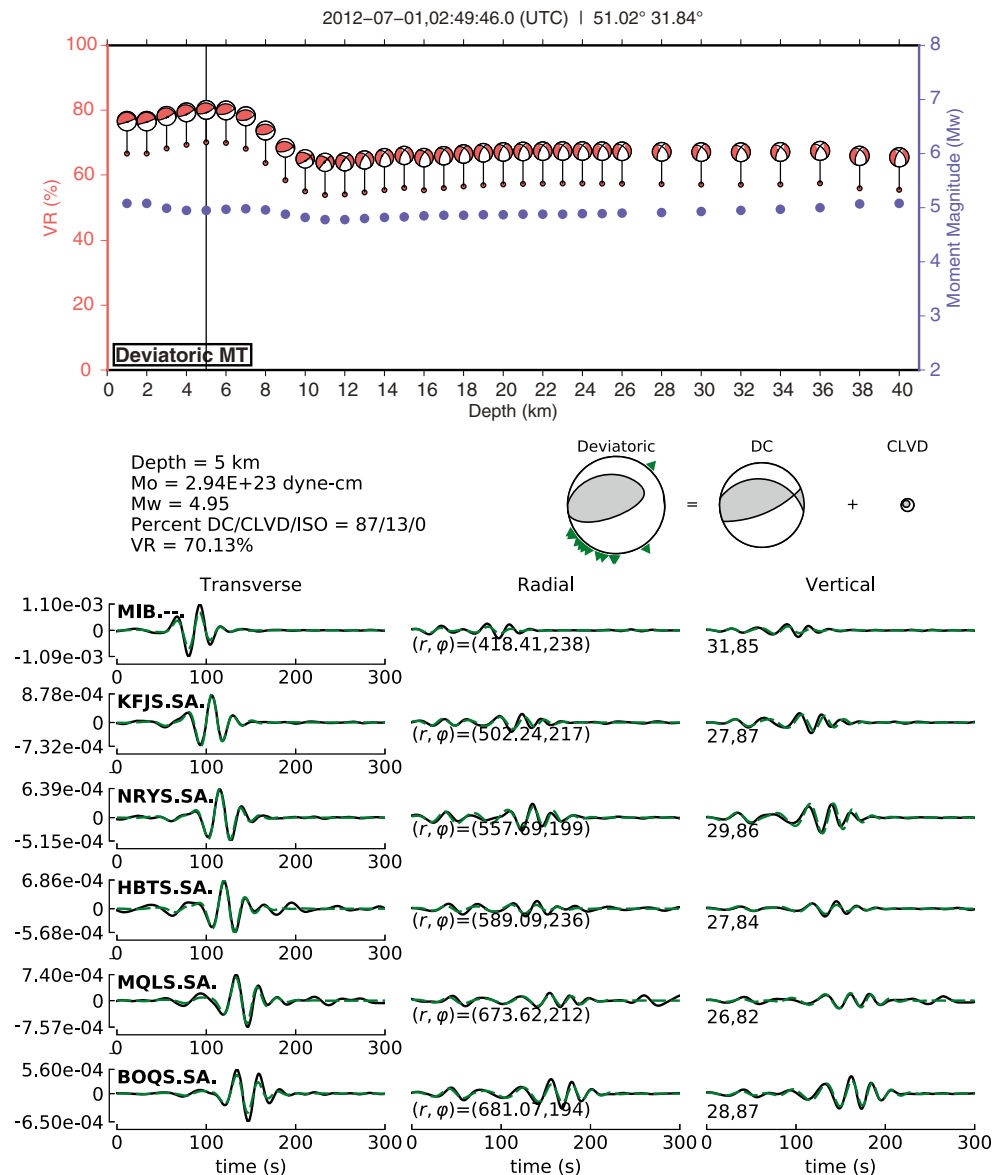
recorded at different stations vary significantly due to the source radiation pattern, source directivity, site conditions, and heterogeneities along the propagation path. On the other hand, coda amplitude measurements have been extensively used to study the source properties of local and regional earthquakes (Mayeda and Walter 1996; Mayeda et al. 2003; Gök et al. 2016), and studies have shown that coda measurements are more stable than direct wave measurements (e.g., Mayeda et al. 2007). We can make amplitude measurements at consecutive narrowband coda envelopes to reconstruct the source spectrum of the earthquake, provided that the coda envelope measurements are corrected for path, site, and S-to-coda transfer functions. The observed coda

envelope function $A_c(f, t, r)$ at a given center frequency f , seconds from origin time t , and epicentral distance r is defined as

$$A_c(f, t, r) = W_0(f) \times S(f) \times T(f) \times P(r, f) \times H\left(t - \frac{r}{v(f, r)}\right) \times \left(t - \frac{r}{v(f, r)}\right)^{-\gamma(f, r)} \exp\left[b(f, r) \times \left(t - \frac{r}{v(f, r)}\right)\right] \quad (1)$$

in which v is the peak velocity, W_0 represents the S-wave source, T represents the S-to-coda transfer function, S is the site effect, P includes the effects of geometrical

Fig. 4 Moment tensor solution of an earthquake in the Zagros Mountains (No. 9). A reverse faulting event in the Zagros Mountain. Top panel shows the solution, in terms of waveform fits (variance reduction; VR) and Mw, with respect to source depth. Bottom panel shows the best solution and waveform fits at selected stations. Green triangles around the beach ball indicate station azimuth, and the numbers below the radial and vertical component seismograms are from left to right: distance, azimuth, time shift in samples, and station-specific VR



spreading and attenuation, H is the Heaviside step function, and $\gamma(r)$ and $b(r)$ are the distance-dependent coda shape factors that control the envelope shape. Mayeda et al. (2003) demonstrated that empirically determined distance-dependent coda envelope shape captures the observed local and regional coda envelope shapes reasonably well. After correcting for source, path, site, and transfer function effects, Eq. 1 becomes

$$\begin{aligned} \log_{10} \left[A_c(f, t, r) \times \left(t - \frac{r}{v(f, r)} \right)^{\gamma(f, r)} \right] \\ = \log_{10} \left[H \left(t - \frac{r}{v(f, r)} \right) \right] + b(f, r) \\ \times \left(t - \frac{r}{v(f, r)} \right) \times \log_{10}(e) \end{aligned} \quad (2)$$

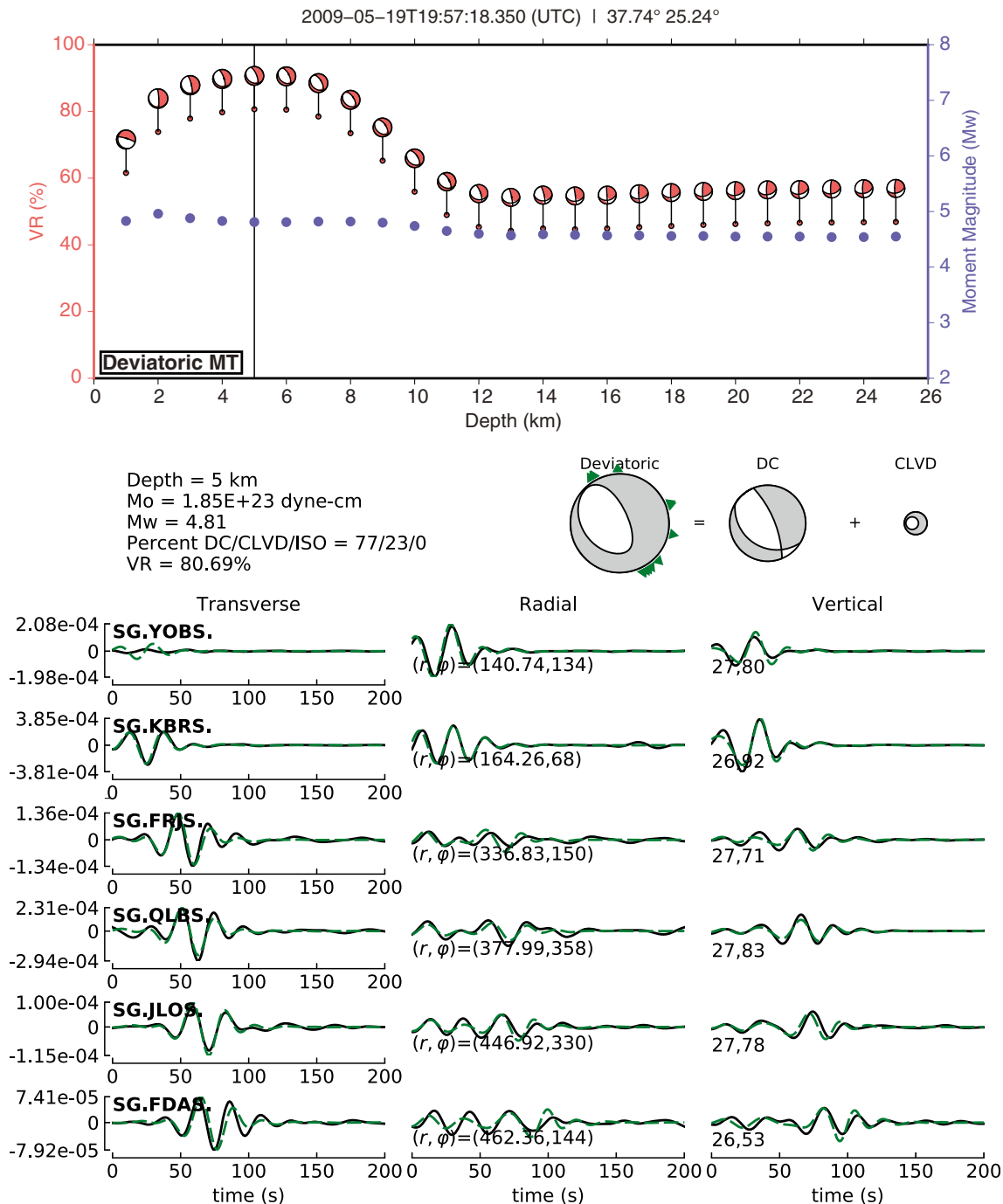


Fig. 5 Moment tensor solution of an earthquake in the Red Sea Region (No. 39). Normal faulting event in the vicinity of the Red Sea Rift Zone. See Fig. 4 caption for details

Details of the path, site, S-to-coda transfer functions, and coda envelope shape functions can be found in (Gök et al. 2016). Here, we highlight the key terms in Eqs. 1 and 2 is implemented in the LLNL-developed, Java-based software application called Coda Calibration Tool (CCT). CCT is developed for calibrating 1D shear wave coda envelopes to a small set of reference events and uses the calibrated envelopes to estimate M_w (<https://github.com/LLNL/coda-calibration-tool>) using velocity seismograms in the north–south and east–west directions and recorded at epicentral distances up to 14° . We compute the narrowband envelope at each frequency band, ranging from 0.03 to 8 Hz, from the Hilbert transform of bandpass-filtered horizontal channel waveforms and stack the envelopes in log space.

After stacking, to obtain the envelope peak velocity function $v(f, r)$, represented by a simple hyperbola, we measure the maximum peak velocity within the group velocity window of 4.7–2.3 km/s. Once a region has been calibrated, $v(f, r)$ can be applied to future measurements in the region. Coda envelope window lengths are determined by manual inspection of the time window of the envelope. The expectation of minimum

and maximum window length was adopted from previous studies and shapes of the coda envelopes are represented by functional forms demonstrated to fit the envelopes as a function of increasing distance at each narrowband frequency. The coda shape parameter does not seem to vary much at local to near regional, although as frequencies increase, the shape parameter seems to show increasing variation at local distances.

Next is the path correction $P(r, f)$ performed using an empirical correction known as the extended Street and Herrmann (ESH) correction where the path correction term can be separated into geometrical spreading and scattering attenuation (Eq. 6 from Gök et al. 2016). The final step of the calibration is to correct for S-to-coda transfer $T(f)$ in Eq. 1 and the relative site effects. This requires independently obtained M_w 's. Large events are preferred to reduce uncertainty caused by imperfect knowledge of the Earth's subsurface structure. We use large earthquakes from Table 2 (Nos. 12, 15, and 16 for Zagros; Nos. 34 and 38 for Red Sea) as reference events for calibration to construct the envelopes, and use the calibrated envelopes to estimate M_w for the rest of the events. In addition, we included apparent stress ($\sigma_a = 0.57$) for Event 12

Fig. 6 Moment tensor solutions of an M_w 3.44 earthquake (No. 41). A small magnitude event located in western Arabian Peninsula just north of Harrat Lunayyir. See Fig. 4 caption for details

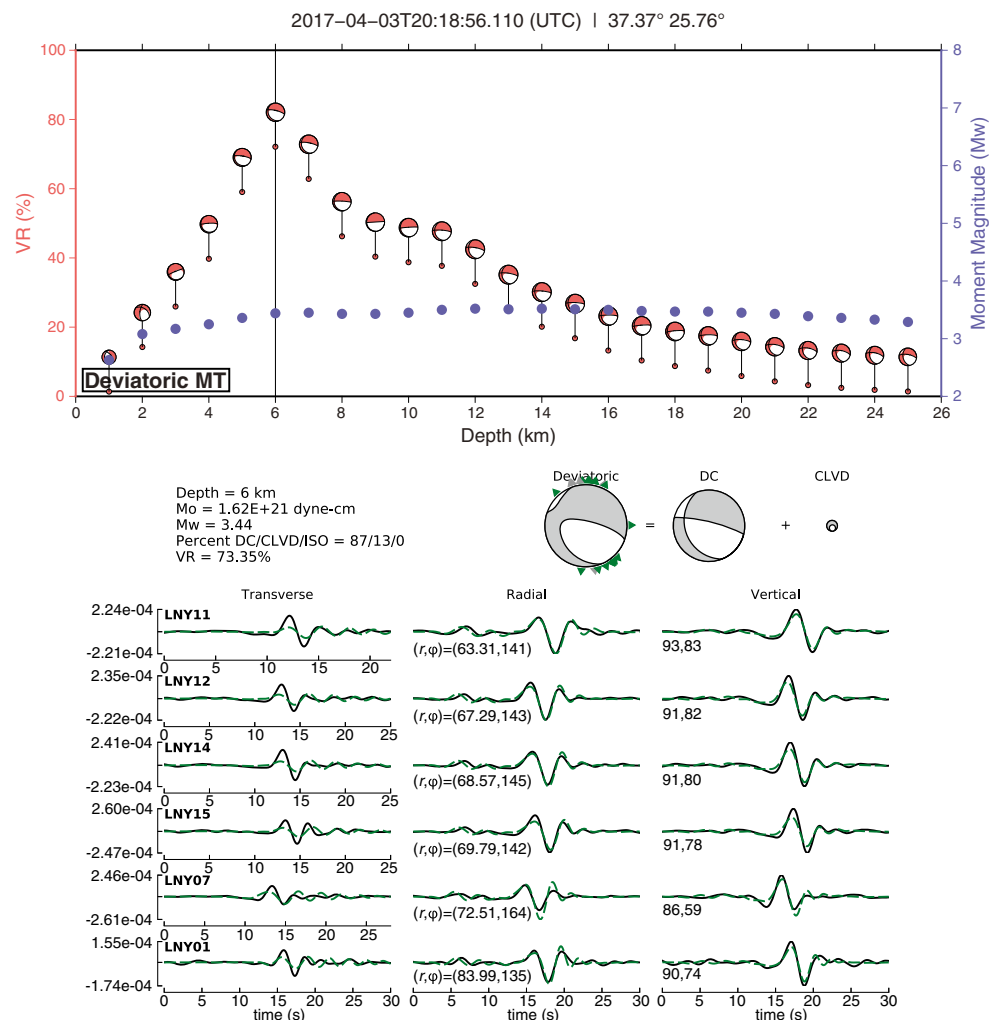
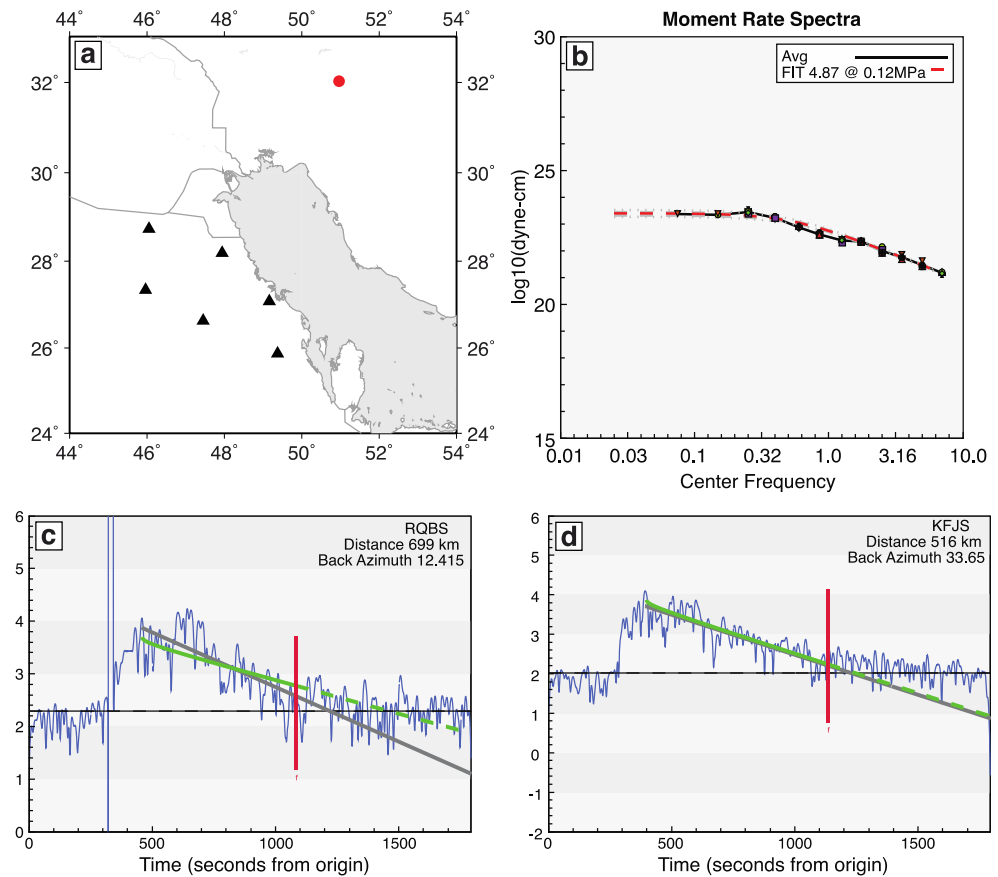


Fig. 7. Zagros coda calibration.

An example calibration result from the Zagros subregion (No. 9; same event in Fig. 4). (a) A map of the event and stations used for calibration. (b) Final source spectra from all six stations in (a). Coda envelopes in the 0.2- to 0.3-Hz frequency band, at stations (c) RQBS and (d) KFJS. Fits to the envelope at the station is in green, averaged fit from all stations are shown in gray, and the red vertical line marks the end time of the envelope measurement



(K. Mayeda, personal communication). Because of the larger epicentral distances, we divide the study area into two calibration subregions to eliminate the 2-D path effects (Fig. 2). The “Red Sea” subregion covers the Red Sea Rift Zone and coastal Arabian Shield; and the “Zagros” subregion includes the Zagros fold-and-thrust belt and the Arabian Platform with thick sedimentary layer in upper crust.

Result: moment tensor solutions

Deviatoric moment tensor solutions for the 46 earthquakes analyzed are shown in Fig. 3. The coverage plays an important role when assessing solution uncertainty; with a few exceptions, the azimuthal coverage is generally limited due to the earthquake and station distributions where half of the

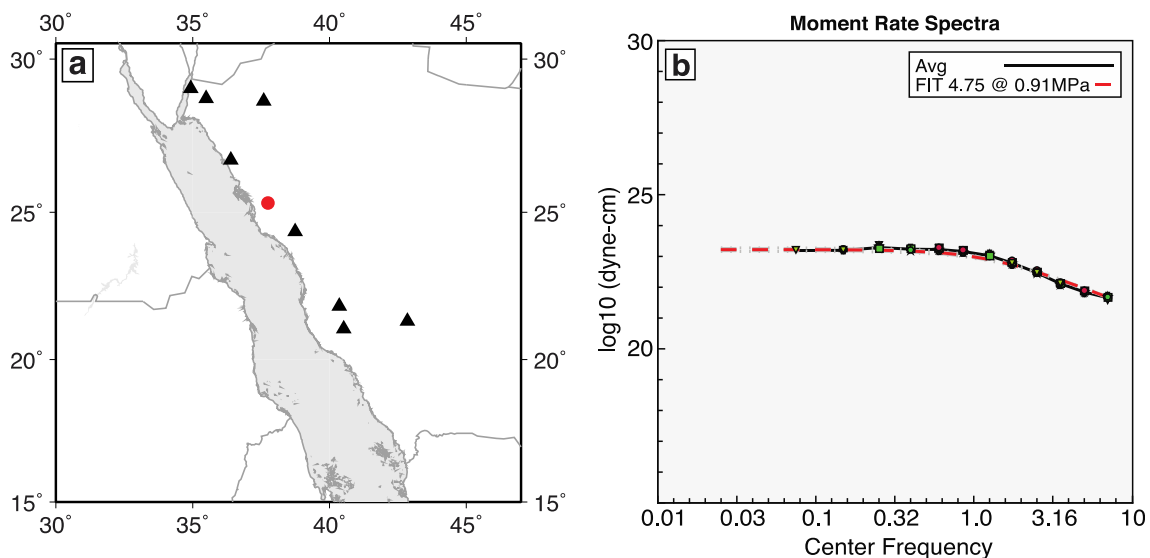


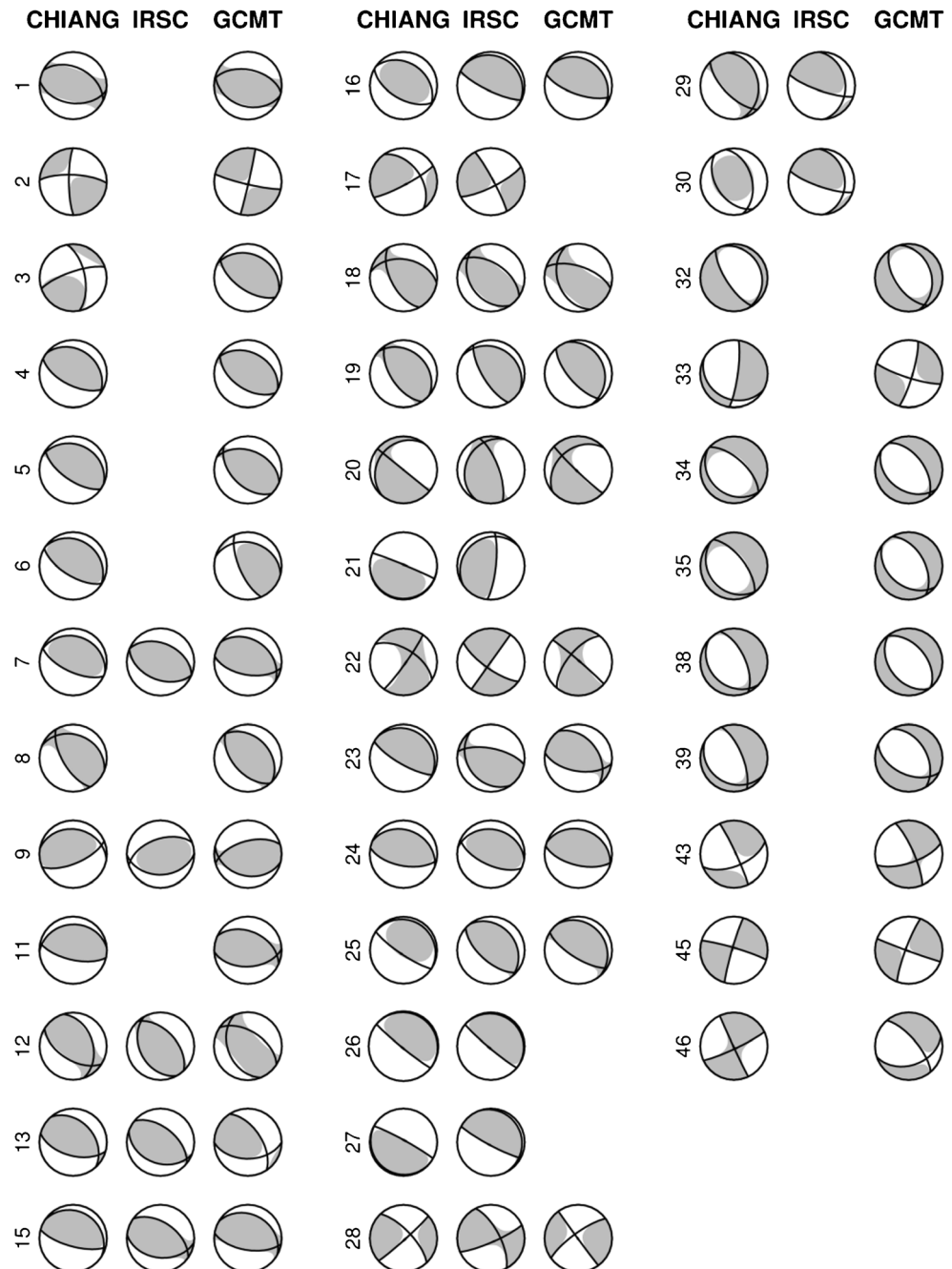
Fig. 8. Red Sea coda calibration. Red Sea calibration provided reasonably robust results and shown here is the resulting source spectra for one of the Lunayyir earthquake (No 39; same event in Figure 5). See Fig. 7 caption for details

earthquakes studied have azimuthal gaps greater than 180° . For instance, depending on the earthquake locations, the station coverage is concentrated on either the west side (Zagros) or east side (Western Arabian Peninsula) of the earthquake populations. Within the Zagros fold-and-thrust belt are mostly reverse-faulting earthquakes where the fault planes are oriented along the NW-SE direction (Fig. 4), consistent with the regional tectonics. Because we are fitting mostly long-period surface waves (0.02 to 0.05 Hz), the inversion is not as sensitive to source depth, nonetheless the depths are mostly distributed within the upper crust (~ 10 km), consistent with an

earlier study on modeling moderate Zagros earthquake using teleseismic depth phases and regional moment tensors (Adams et al. 2009) and solutions from the Iranian Seismological Center (IRSC) centroid moment tensor catalog (Hosseini et al. 2019).

In contrast to the Zagros fold-and-thrust belt, the northwestern Arabian Peninsula is not as seismically active but does have occasional earthquake swarms associated with Quaternary volcanic fields (Pallister et al. 2010; Mukhopadhyay et al. 2013). We received data for four earthquakes that were part of the 2009 Harrat Lunayyir earthquake swarm (Nos. 36 to 39), including the

Fig. 9 Focal mechanism comparisons. Comparison of focal mechanisms from deviatoric moment tensor inversion between this study, solutions published by Iranian Seismological Center (IRSC) and Global Centroid-Moment-Tensor (GCMT). Numbers for each row correspond to the numbers in the first column of Table 2



largest M_b 5.7 event that occurred on May 19, 2009 which was associated with a northwest-trending 8-km-long surface rupture across the northern section of the Harrat. Pallister et al. (2010) modeled the surface deformation as an NNW-trending, 10 km-long shallow dike intrusion using InSAR. All of the earthquake full moment tensor solutions have negligible isotropic components, suggesting they are unlikely to have volume change associated with rock failure, and are located at depths between 4 and 8 km. The Lunayyir earthquakes also do not have anomalous CLVD mechanisms that can be interpreted as ring faulting, such as some of the large, non-double-earthquakes with dominant vertical tension or pressure axes detected globally (Shuler et al. 2013). Out of the four earthquakes, three of them have normal-faulting mechanisms and the smallest M_w 3.8 earthquake (No. 36) has a strike-slip mechanism. Magmatic dike intrusions in volcanic rift zones are often accompanied by normal and occasionally strike-slip faulting (Ágústsson et al. 2016) on the surface. The seismicity pattern is variable and are strongly influenced by pre-existing conditions such as the local and regional stress state and material properties (Rubin and Pollard 1988; Rubin 2012). Moment tensor solutions from the 2009 Harrat Lunayyir swarm are similar to previously published focal mechanisms from first motion data (Pallister et al. 2010; Hansen et al. 2013) and the Global Centroid-Moment-Tensor (GCMT) catalog (Dziewonski et al. 1981; Ekström et al. 2012). Like earthquakes located at Harrat Lunayyir, a few other earthquakes along the western Arabian Shield all have normal and strike-slip mechanisms with little isotropic components. These earthquakes are most likely also a result of the broader rift-related extension along the Red Sea Rift Zone. In addition to on-shore seismicity, we also examined five earthquakes in the Red Sea in which one of the moment tensor solutions has an anomalous reverse mechanism at 18-km depth. Spreading centers typically have normal- and strike-slip faulting occurring at the shallow crust due to the tectonic stress conditions (Huang and Solomon 1987). All Red Sea events have fewer stations, and very limited azimuthal coverage due to the lack of access to data on the west side of the rift zone (Fig. 5). Increasing azimuthal coverage particularly for the small- to moderate-sized earthquakes will provide more confidence in the retrieved solution. An example of excellent station coverage is an earthquake just north of Harrat Lunayyir (Fig. 6) where we are able to obtain robust moment tensor solution of a M_w 3.4 event (No. 41) using local and regional distance stations.

Result: moment magnitudes from coda envelopes

For Zagros calibration, we have 29 events recorded by 32 stations at the eastern part of the country. Thick sediments in Mesopotamia cause a secondary peak in the coda envelopes from 0.2 to 0.3 Hz (Fig. 7) with a maximum peak around 1.5

km/s. Sedimentary layer geometry or waveguide results in different behavior in the coda envelopes, so the peaking is not universally prominent across all stations. This results in a slight peaking in the coda source spectra at some stations. This effect is carefully examined in all station-event pairs to verify that the final, constructed source spectra are not biased by the peaking. We exclude these stations with strong peaking in the coda envelopes to reduce their impact on the subsequent magnitude estimation. Figure 7 shows waveforms from event

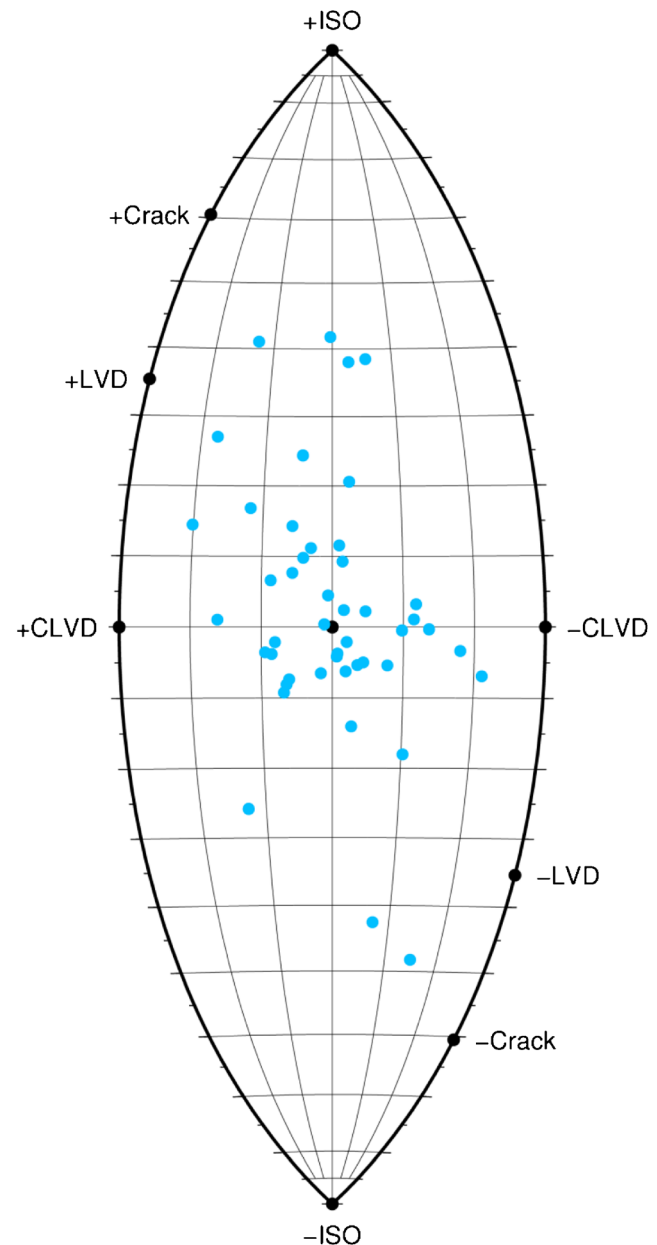


Figure 10. Earthquake source types. Earthquake source types inferred from full moment tensor solutions, based on the geometric framework of moment tensors on a three-dimensional unit sphere (Tape and Tape 2012). Theoretical double-couple (earthquake) sources plot at the center of the lune, and positions of other theoretically source types are labelled as well

No. 9 recorded along the E-W direction at two different stations, where we see trapped secondary surface waves at station RQBS and a more stable envelope at station KFJS. For this event, the final source spectra of six stations show remarkably similar result.

Unlike the Zagros calibration, we have a much smaller set of earthquakes in the Red Sea subregion to estimate coda M_w , but in total, we have 6 events recorded by more than 100 stations. Because the Red Sea calibration spans a much wider distance, including more complex velocity and Q structure, path effect caused higher variation at higher frequencies in the Red Sea subregion than at Zagros. The path effects are possibly due to higher attenuation in the upper mantle of the Arabian Shield. Nonetheless, the coda calibration technique still produces reasonably robust results. Figure 8 shows remarkably similar final source spectra at most frequency bands and across large epicentral distances, with higher scatter in spectral shape above the 1.5- to 2.0-Hz frequency band.

Discussion

The addition of SNSN data drastically increased the number of waveforms available for source characterization; however, the distribution of earthquakes meant the increase in data coverage is mostly along epicentral distances and not azimuthal coverage. Particularly for moment tensor inversions, better azimuthal coverage results in more dense sampling of the radiation pattern. To gain confidence and additional insight in our solutions, we compared moment tensor solutions from this study to other solutions using teleseismic body and surface waves (GCMT) and regional waveform solutions from the IRSC catalog (Fig. 9); the latter has

a denser regional network available for monitoring earthquakes within Iran (e.g., Zagros). In most cases, the source mechanisms are similar amongst the different catalogs. Variability in the focal mechanism is mostly from differences in double-couple or oblique components between different catalog solutions. However, there are two earthquakes in the Zagros (Nos. 21 and 27) where our mechanisms disagree with the IRSC solutions. These earthquakes are part of a population that deviates further from a theoretical double-couple source type (Fig. 10) and our inversion places these earthquakes at a very shallow depth of 2 km. Event 27 is of particular interest because there are discrepancies in source depth and M_w . The IDC (International Data Centre) and IRSC catalogs estimated the event to be deeper, 16.5 km and 26 km, respectively. Moment tensor-derived M_w is also much higher than coda M_w and IRSC M_w compared to other earthquakes analyzed in this study. The discrepancies suggest that the velocity model used in waveform modeling may need refinement to better account for deeper structure. Earthquake populations tend to have much greater scatter in source-type space compared to other event types (i.e., mine collapses) partly because we have many more earthquake measurements. Azimuthal coverage and Earth model uncertainty contribute to most of the scatter. We have less constraint on the retrieved moment tensor solution when we do not have good station coverage that samples the entire focal sphere, and when we do not have well-calibrated velocity models. We used a velocity model that tries to capture the average structure across the Arabian Peninsula because that is where most stations are located, but this model may not be adequate enough to be used along the entire Zagros fold-and-thrust belt. In terms of M_w , estimates between our study and the regional solutions from IRSC (Fig. 11a) agree much better than compared to GCMT (Fig. 11b). M_w

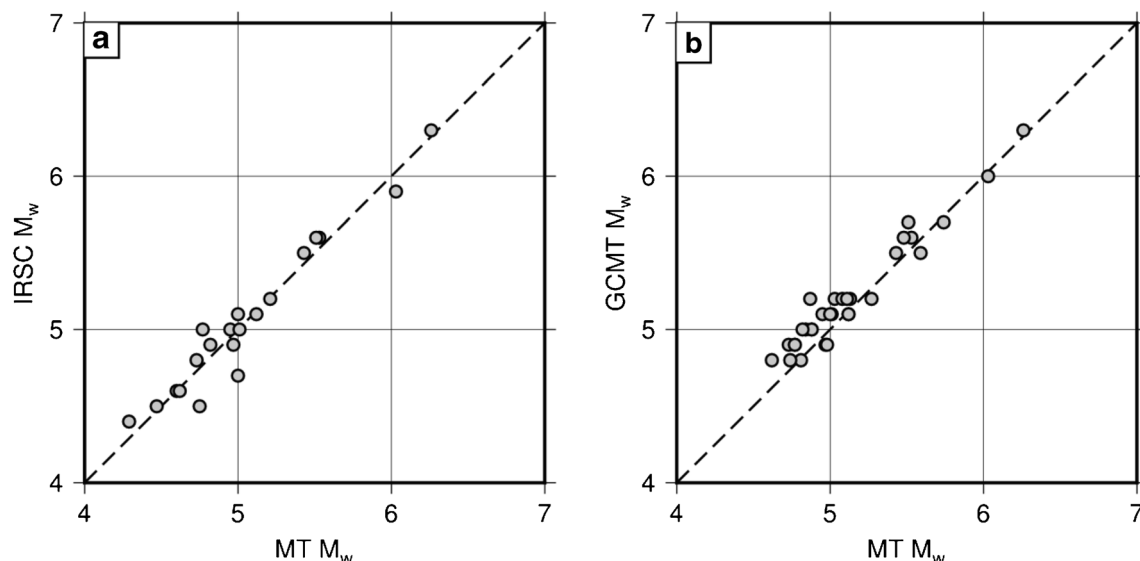


Fig. 11. Moment magnitudes from waveform inversion. Comparing moment tensor-derived moment magnitude (MT M_w) between this study and (a) Zagros fold-and-thrust belt earthquakes from Iranian

Seismological Center (IRSC) and (b) earthquakes from the Global Centroid-Moment-Tensor (GCMT)

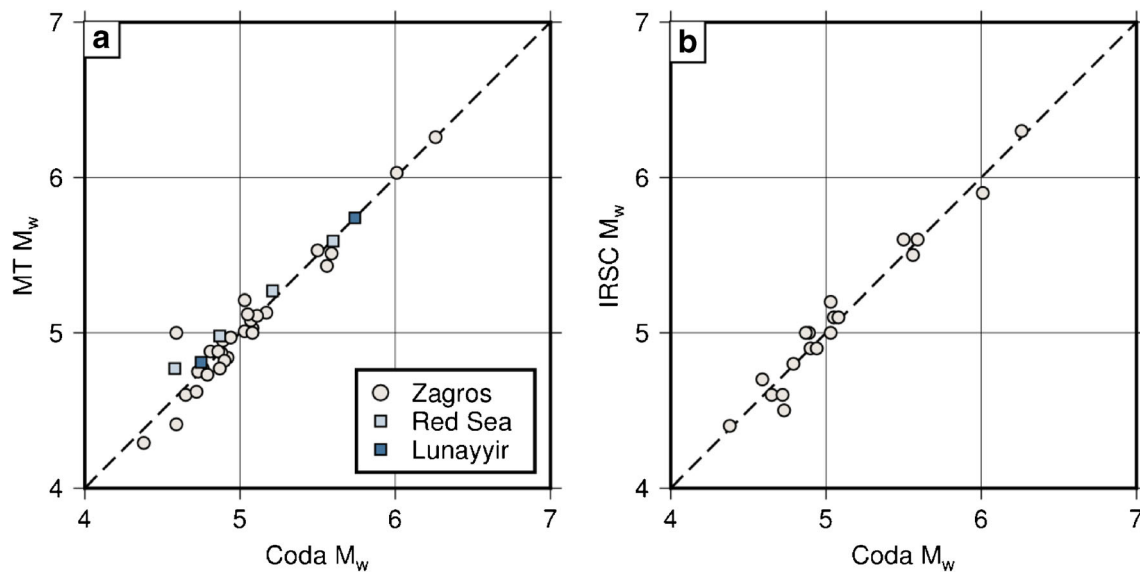


Fig. 12 Coda magnitudes. Comparing coda moment magnitude (coda M_w) to moment tensor M_w from (a) this study and (b) Iranian Seismological Center (IRSC)

computed using long-period teleseismic waveforms tend to be greater than regional moment estimates as most measurements are above the 1:1 linear trend. Theoretically, moment tensor inversion of seismic events at shallow depth can lead to bias in seismic moment because the M_{xz} , M_{yz} , and M_{zz} components of the tensor are poorly resolved. This bias is due to vanishing traction near the free surface, as the source depth approaches the free surface the basis Green's functions for these moment tensor components go to zero (Chiang et al. 2016). This bias in moment can be exacerbated when longer period waveforms are used because the wavelength of the data compared to the source dimension increases.

The analysis of stable coda envelope amplitudes compared with regional moment tensor solutions provides an independent check on scalar seismic moment biases, as well as biases in the source mechanism. Coda envelopes are not as sensitive to 3D propagation path effects and source radiation due to the scattering nature of coda waves, which averages out path and source variations over long distances (Mayeda and Malagnini 2010; Gök et al. 2016). Figure 12a shows the comparison between deviatoric moment tensor M_w and coda M_w . Excluding the three reference events, the average difference in M_w between the two methods is 0.08 with a standard deviation of 0.08. There is scatter in the M_w 's but mostly due to the previously discussed problematic Zagros earthquake (No. 27). If we consider the mean differences, commonly, these types of comparisons are expected to be within ± 0.1 magnitude units from most M_w catalogs. The independently derived coda magnitude estimates for the 32 earthquakes are slightly less than ± 0.1 between the two methods in this study. In addition, coda M_w 's are also very comparable to M_w estimates by IRSC (Fig. 12b) with a mean difference of 0.07 and a standard deviation of 0.08. This give

us confidence that we are producing stable and robust M_w estimates from coda envelopes.

Conclusions

We perform moment tensor inversion on 46 earthquakes and coda envelope calibration on 35 earthquakes from the Zagros Mountains to the Red Sea using regional seismic data from the Kingdom of Saudi Arabia. For moment tensor inversion, we included additional data from openly available global and regional networks to increase data coverage. Moment tensor solutions reveal different mechanisms for different tectonic environments as expected. With a few exceptions, solutions from this study agree with other published solutions even though our study area spans quite a vast and complex tectonic setting. With the addition of SNSN regional data and path-specific 1D velocity models, we are able to recover reasonably robust source properties. In some cases where events are located within the Arabian Peninsula, hence within the SNSN network, we can lower the magnitude threshold for inversion and still obtain good solutions for these earthquakes. The magnitude threshold for moment tensor inversion depends on the signal-to-noise ratio of the data and our knowledge of the subsurface velocity structure. In this study, most of the surface waves have clear signals in the intermediate- to long-period passband (0.02 to 0.1 Hz), and can be modeled by well-calibrated 1D Earth models. In terms of M_w 's, we have good agreement between coda-derived and moment tensor-derived M_w 's, with the exception of one problematic event where source depth is not well constrained by moment tensor inversion. It is particularly important for our study to check for any potential bias in the moment tensor solution

because the majority of earthquakes are located outside of the SNSN network and in very different tectonic environments. Coda magnitudes provided independent validation of the scalar seismic moment with no indication of model bias or relatively unfavorable station coverage. Coda Mw for Zagros events are also very comparable to estimates from the IRSC catalog, which gives us confidence that we are producing stable and robust Mw estimates from coda envelopes, as well as from moment tensor inversion. Access to high-quality waveform data from well-calibrated regional seismic stations is one of the key requirements in producing robust and stable estimates of earthquake source parameters. Utilizing data from neighboring networks around the Arabian Peninsula can significantly reduce the azimuthal gap and is especially important to increase confidence in estimating source properties for the majority of earthquakes occurring outside the SNSN network. Identifying source parameters are essential for not only understanding the seismotectonics of Arabian Peninsula. Coda-based magnitude studies with the use of Java-based CCT tool provide a set of calibration parameters for both regions which can now be used for rapid calculations in routine operations at SGS using the SNSN network.

Acknowledgments Lawrence Livermore National Laboratory is operated by Lawrence Livermore National Security, LLC, for the U.S. Department of Energy, National Nuclear Security Administration under Contract DE-AC52-07NA27344. This is LLNL contribution LLNL-JRNL-1013470. We would like to thank the two anonymous reviewers for their valuable feedback and efforts toward improving our manuscript.

Funding This study has been financially prepared by LLNL under Contract DE-AC52-07NA27344.

Data availability Saudi National Seismic Network (SNSN) waveforms are closed and are provided by the Saudi Geological Survey. Publicly available waveforms and metadata are archived at the Incorporated Research Institutions for Seismology (IRIS; last accessed online June 17, 2019). Land topography and ocean bathymetry come from ETOPO1 Global Relief Model (Amante and Eakins 2009). Waveform plots were generated using Python libraries Obspy and MoPaD. Maps and source-type plots were made using the Generic Mapping Tools 5.4.4 last accessed on July 2019 (Wessel et al. 2013).

Compliance with ethical standards

Conflict of interest The authors declare that they have no conflict of interest.

Ethics approval Not applicable.

Consent to participate Not applicable.

Consent for publication Not applicable.

Code availability Moment tensor inversion and the Coda Calibration Tool are available online at <https://github.com/LLNL/tldmtpy> and <https://github.com/LLNL/coda-calibration-tool>, respectively.

References

- Adams A, Brazier R, Nyblade A, Rodgers A, al-Amri A (2009) Source parameters for moderate earthquakes in the Zagros Mountains with implications for the depth extent of seismicity. *Bull Seismol Soc Am* 99:2044–2049. <https://doi.org/10.1785/0120080314>
- Ágústssdóttir T, Woods J, Greenfield T, Green RG, White RS, Winder T, Brandsdóttir B, Steinthórsson S, Soosalu H (2016) Strike-slip faulting during the 2014 Bárðarbunga-Holuhraun dike intrusion, central Iceland. *Geophys Res Lett* 43:1495–1503. <https://doi.org/10.1002/2015GL067423>
- Amante C, Eakins BW (2009) ETOPO1 1 Arc-minute global relief model: procedures, data sources and analysis. National Centers for Environmental Information, NESDIS, NOAA, U.S. Department of Commerce
- Berberian M (1981) Active faulting and tectonics of Iran. In: Zagros, Hindu Kush, Himalaya: geodynamic evolution. American Geophysical Union (AGU), Washington, D.C, pp 33–69. <https://doi.org/10.1029/GD003p0033>
- Camp VE, Roobol MJ (1992) Upwelling asthenosphere beneath western Arabia and its regional implications. *J Geophys Res Solid Earth Planets* 97:15255–15271. <https://doi.org/10.1029/92JB00943>
- Camp VE, Hooper PR, Roobol MJ, White DL (1987) The Madinah eruption, Saudi Arabia: magma mixing and simultaneous extrusion of three basaltic chemical types. *Bull Volcanol* 49:489–508
- Chiang A, Dreger DS, Ford SR, Walter WR, Yoo SH (2016) Moment tensor analysis of very shallow sources. *Bull Seismol Soc Am* 106: 2436–2449. <https://doi.org/10.1785/0120150233>
- Chiang A, Ichinose GA, Dreger DS, Ford SR, Matzel EM, Myers SC, Walter WR (2018) Moment tensor source-type analysis for the Democratic People's Republic of Korea—Declared Nuclear Explosions (2006–2017) and 3 September 2017 Collapse Event. *Seismol Res Lett* 89:2152–2165. <https://doi.org/10.1785/0220180130>
- Cong L, Mitchell BJ (1999) Lg Coda Q and its relation to the geology and tectonics of the Middle East. In: Mitchell BJ, Romanowicz B (eds) *Q of the Earth: Global, Regional, and Laboratory Studies*. Birkhäuser Basel, Basel, pp 563–585
- Dreger DS (2003) 85.11 - TDMT_INV: Time domain seismic moment tensor inversion. In: Lee WHK, Kanamori H, Jennings PC, Kisslinger C (eds) *International geophysics Volume 81, Part B*. Academic Press, Cambridge, p 1627. [https://doi.org/10.1016/S0074-6142\(03\)80290-5](https://doi.org/10.1016/S0074-6142(03)80290-5)
- Dziewonski AM, Chou TA, Woodhouse JH (1981) Determination of earthquake source parameters from waveform data for studies of global and regional seismicity. *J Geophys Res Solid Earth* 86: 2825–2852. <https://doi.org/10.1029/JB086iB04p02825>
- Ekström G, Nettles M, Dziewonski AM (2012) The global CMT project 2004–2010: Centroid-moment tensors for 13,017 earthquakes. *Phys Earth Planet Inter* 200–201:1–9. <https://doi.org/10.1016/j.pepi.2012.04.002>
- Ford SR, Dreger DS, Walter WR (2009) Identifying isotropic events using a regional moment tensor inversion. *J Geophys Res Solid Earth* 114:112. <https://doi.org/10.1029/2008JB005743>
- Gök R, Kaviani A, Matzel EM, Pasyanos ME, Mayeda K, Yetirmishli G, el-Hussain I, al-Amri A, al-Jeri F, Godoladze T, Kalafat D, Sandvol EA, Walter WR (2016) Moment magnitudes of local/regional events from 1D coda calibrations in the Broader Middle East Region moment magnitudes of local/regional events from 1D coda calibrations in the broader Middle East Region. *Bull Seismol Soc Am* 106:1926–1938
- Hansen SE, Rodgers AJ, Schwartz SY, Al-Amri AMS (2007) Imaging ruptured lithosphere beneath the Red Sea and Arabian Peninsula. *Earth Planet Sci Lett* 259:256–265. <https://doi.org/10.1016/j.epsl.2007.04.035>

- Hansen SE, DeShon HR, Moore-Driskell MM, Al-Amri AMS (2013) Investigating the P wave velocity structure beneath Harrat Lunayyir, northwestern Saudi Arabia, using double-difference tomography and earthquakes from the 2009 seismic swarm. *J Geophys Res Solid Earth* 118:4814–4826. <https://doi.org/10.1002/jgrb.50286>
- Herrmann RB (2013) Computer programs in seismology: an evolving tool for instruction and research. *Seismol Res Lett* 84:1081–1088
- Hosseini H, Pakzad M, Naserieh S (2019) Iranian regional centroid moment tensor catalog: Solutions for 2012–2017. *Phys Earth Planet Inter* 286:29–41. <https://doi.org/10.1016/j.pepi.2018.11.001>
- Huang PY, Solomon SC (1987) Centroid depths and mechanisms of mid-ocean ridge earthquakes in the Indian Ocean, Gulf of Aden, and Red Sea. *J Geophys Res Solid Earth* 92:1361–1382. <https://doi.org/10.1029/JB092iB02p01361>
- Jost ML, Herrmann RB (1989) A student's guide to and review of moment tensors. *Seismol Res Lett* 60:37–57. <https://doi.org/10.1785/gssrl.60.2.37>
- Mayeda K, Malagnini L (2010) Source radiation invariant property of local and near-regional shear-wave coda: application to source scaling for the Mw5.9 Wells, Nevada sequence. *Geophys Res Lett* 37:n/a–n/a. <https://doi.org/10.1029/2009GL042148>
- Mayeda K, Walter WR (1996) Moment, energy, stress drop, and source spectra of western United States earthquakes from regional coda envelopes. *J Geophys Res Solid Earth* 101:11195–11208. <https://doi.org/10.1029/96JB00112>
- Mayeda K, Hofstetter A, O'Boyle JL, Walter WR (2003) Stable and transportable regional magnitudes based on coda-derived moment-rate spectra. *Bull Seismol Soc Am* 93:224–239. <https://doi.org/10.1785/0120020020>
- Mayeda K, Malagnini L, Walter WR (2007) A new spectral ratio method using narrow band coda envelopes: evidence for non-self-similarity in the Hector Mine sequence. *Geophys Res Lett* 34. <https://doi.org/10.1029/2007GL030041>
- Minson SE, Dreger DS (2008) Stable inversions for complete moment tensors. *Geophys J Int* 174:585–592. <https://doi.org/10.1111/j.1365-246X.2008.03797.x>
- Mitchell BJ, Pan Y, Xie J, Cong L (1997) Lg coda Q variation across Eurasia and its relation to crustal evolution. *J Geophys Res Solid Earth* 102:22767–22779. <https://doi.org/10.1029/97JB01894>
- Mouthereau F, Lacombe O, Vergés J (2012) Building the Zagros collisional orogen: timing, strain distribution and the dynamics of Arabia/Eurasia plate convergence. *Tectonophysics* 532–535:27–60. <https://doi.org/10.1016/j.tecto.2012.01.022>
- Mukhopadhyay B, Mogren S, Mukhopadhyay M, Dasgupta S (2013) Incipient status of dyke intrusion in top crust – evidences from the Al-Ays 2009 earthquake swarm, Harrat Lunayyir, SW Saudi Arabia. *Geomat Nat Haz Risk* 4:30–48. <https://doi.org/10.1080/19475705.2012.663794>
- Nayak A, Dreger DS (2018) Source inversion of seismic events associated with the Sinkhole at Napoleonville Salt Dome, Louisiana using a 3D velocity model. *Geophys J Int*. <https://doi.org/10.1093/gji/ggy202>
- Pallister JS, McCausland WA, Jónsson S et al (2010) Broad accommodation of rift-related extension recorded by dyke intrusion in Saudi Arabia. *Nat Geosci* 3:705–712. <https://doi.org/10.1038/ngeo966>
- Pasyanos ME, Walter WR, Flanagan MP et al (2004) Building AND TESTING an *a priori* geophysical model for Western Eurasia and North Africa. *Pure Appl Geophys* 161:235–281. <https://doi.org/10.1007/s00024-003-2438-5>
- Pollastro RM, Karshbaum AS, Viger RJ (1999) Maps showing geology, oil and gas fields and geologic provinces of the Arabian Peninsula. USGS Open-File Report
- Regard V, Bellier O, Thomas JC, et al (2004) Accommodation of Arabia-Eurasia convergence in the Zagros-Makran transfer zone, SE Iran: a transition between collision and subduction through a young deforming system. *Tectonics* 23:n/a–n/a. <https://doi.org/10.1029/2003TC001599>
- Reilinger R, McClusky S, Vernant P, Lawrence S, Ergintav S, Cakmak R, Ozener H, Kadirov F, Guliev I, Stepanyan R, Nadariya M, Hahubia G, Mahmoud S, Sakr K, ArRajehi A, Paradissis D, al-Aydrus A, Prilepin M, Guseva T, Evren E, Dmitrova A, Filikov SV, Gomez F, al-Ghazzi R, Karam G (2006) GPS constraints on continental deformation in the Africa-Arabia-Eurasia continental collision zone and implications for the dynamics of plate interactions. *J Geophys Res Solid Earth* 111. <https://doi.org/10.1029/2005JB004051>
- Rodgers AJ, Ni JF, Hearn TM (1997) Propagation characteristics of short-period Sn and Lg in the Middle East. *Bull Seismol Soc Am* 87:396–413
- Rodgers AJ, Walter WR, Mellors RJ, al-Amri AMS, Zhang YS (1999) Lithospheric structure of the Arabian shield and platform from complete regional waveform modelling and surface wave group velocities. *Geophys J Int* 138:871–878
- Rubin AM (2012) Dike-induced faulting and graben subsidence in volcanic rift zones. *J Geophys Res Solid Earth* 97:1839–1858. <https://doi.org/10.1029/91JB02170>
- Rubin AM, Pollard DD (1988) Dike-induced faulting in rift zones of Iceland and Afar. *Geology* 16:413–417
- Shuler A, Ekström G, Nettles M (2013) Physical mechanisms for vertical-CLVD earthquakes at active volcanoes. *J Geophys Res Solid Earth* 118:1569–1586. <https://doi.org/10.1002/jgrb.50131>
- Stoeser DB, Camp VE (1985) Pan-African microplate accretion of the Arabian Shield. *GSA Bull* 96:817–826
- Tape W, Tape C (2012) A geometric setting for moment tensors. *Geophys J Int* 190:476–498. <https://doi.org/10.1111/j.1365-246X.2012.05491.x>
- Wessel P, Smith WHF, Scharroo R, Luis J, Wobbe F (2013) Generic mapping tools: improved version released. *EOS Trans Am Geophys Union* 94:409–410. <https://doi.org/10.1002/2013EO450001>